Engineering Geology, 35 (1993) 49–64
Elsevier Science Publishers B.V., Amsterdam

Transient poroelastic response of equivalent porous media over a mining panel

Mao Bai[a]* and Derek Elsworth[b]

[a]*School of Petroleum and Geological Engineering The University of Oklahoma Norman, OK 73019-0628, U.S.A.*
[b]*Department of Mineral Engineering The Pennsylvania State University University Park, PA 16802, U.S.A.*

(Received May 25, 1992; revised version accepted March 25, 1993)

ABSTRACT

A transient poroelastic formulation based on the Biot consolidation theory is presented to study the impact of underground longwall mining of coal on strata deformation and the subsequent modification of hydrogeological properties. A finite-element model is used where the geometric conditions may be complex. The important parameters in this model are identified as pore pressure ratio, α_1 and relative compressibility, α_2 with the latter exerting far greater influence on the resulting fluid pressure field than the former. This study indicates that the fluid pressure distribution is strongly controlled by the stress distribution, or the strata deformation induced by mining has a great impact on the change in hydrogeological environment in the mining region.

Introduction

Flow systems in porous media are often transient, resulting in changes in hydraulic head or pore pressures and corresponding mass fluxes with time. This behavior may result from changes in either fluid pressure or total stress boundary conditions applied to the system. It is the admissibility of changes in total stress within the system that describes the essence of coupled poroelastic behavior and sets it apart from decoupled diffusive (flow) systems. Comprehensive coupling between stresses and pore pressures was first rationalized by Biot (1941) and later adopted in many applications to specific poroelastic systems (Ghaboussi and Wilson, 1973; Zienkiewicz et al., 1977; Simon et al., 1984). The poroelastic theory has been applied to problems of consolidation (Booker and Small, 1987), prediction of surface subsidence caused by groundwater extraction (Lewis and Schrefler, 1987) and evaluation of the stress, pressure and failure fields around boreholes (Detournay and Cheng, 1988), among others. This study applies Biot's theory to mining-related problems, evaluating the coupled transient pore pressure response and solid displacement fields that develop as a result of underground mining. Of particular interest is the effect of mining on the behavior of overlying strata where transient pore pressure changes may aid future evaluation of failure around the excavation or alternatively define the mechanical properties of the deforming system.

Poroelastic response

For transient flow systems, the ability of water to be removed from or added to storage within the porous medium controls the rate of response. Specific storage controls this process and may be defined as:

$$S_e = \rho g \left(\frac{1}{K_s} + \alpha_s + \beta_f \right) \quad (1)$$

where ρ is fluid density, g is gravitational acceleration, K_s is bulk modulus of the skeleton of the porous medium, α_s is compressibility of the solid grains and is equal to $(1-n)/K_g$ where n is porosity and K_g is solid bulk modulus of the grains, and β_f

0013-7952/93/$06.00

NOTATION
(M = mass, L = length, t = time)

a^*	load width	L	t	real time	t
a,b	half width and length of element	L	Δt	time increment	t
			T	dimensionless time factor	—
B	strain-displacement matrix	—	u	displacement	L
C_v	consolidation coefficient	L^2t^{-1}	V_i	flow velocity	Lt^{-1}
E	elastic modulus	$ML^{-1}t^{-2}$	V	domain volume	L^{-3}
F	applied boundary tractions	—	x,y	distances	L
f	nodal force	MLt^{-2}	α	pore pressure ratio	—
G	shear modulus	$ML^{-1}t^{-2}$	α_1	pore pressure ratio	—
g	gravitational acceleration	Lt^{-2}	α_2	relative compressibility	—
H,R	Biot constant	—	α_s	compressibility of solid grains	—
H_c	height of column	L	β_f	fluid compressibility	—
h	hydraulic head	L	ε	normal strain	—
K	hydraulic conductivity	Lt^{-1}	ε_{kk},θ	volumetric strain	—
K_s	skeletal modulus	$ML^{-1}t^{-2}$	σ,σ_e	stress, effective stress	$ML^{-1}t^{-2}$
K_f	fluid bulk modulus	$ML^{-1}t^{-2}$	σ_{kk},σ_e	total stress	$ML^{-1}t^{-2}$
K_g	grain bulk modulus	$ML^{-1}t^{-2}$	η,ψ	mapping coordinates	—
n	porosity	—	ρ	fluid density	ML^{-3}
N,M	element based shape functions	—	λ	Lame constant	—
p	fluid pressure	$ML^{-1}t^{-2}$	ν	Poisson ratio	—
Q	boundary discharge	—	ω_0	poroelastic constant	—
q	specific discharge	L^3t^{-1}	ω	overrelaxation factor	—
S	domain surface	L^2	γ	fluid unit weight	$ML^{-2}t^{-2}$
S_e	specific storage	L^2t^{-2}	δ	Kronecker delta	—
S_s	specific surface	L^{-1}	χ	weighting constant	—

is fluid compressibility given by n/K_f with K_f being fluid bulk modulus.

Combining Darcy's law together with continuity requirements, assuming a constant fluid density and considering solid compression due to total stress changes, yields a flow equation of the form:

$$-\nabla(K\nabla h) = -(\alpha_s + \beta_f)\dot{p} + \omega_0\dot{\varepsilon}_{kk} \tag{2}$$

where K is hydraulic conductivity, h is the hydraulic head (pressure head plus elevation head), p is the fluid pressure, ε_{kk} is total volumetric strain, and ω_0 is a constant. Neglecting the influence of time dependent changes in elevation head enables pore fluid pressure to be defined as $p=\rho gh$. Substituting for head in Eq. 2 yields:

$$-\frac{1}{\rho g}\nabla(K\nabla p) = -(\alpha_s + \beta_f)\dot{p} + \omega_0\dot{\varepsilon}_{kk} \tag{3}$$

In this equation specific storage is in a form representing the compressibility of fluid and solid grains with skeletal compressibility encompassed in the term ω_0.

The general stress–strain relationship incorporating effective stress effects through pore pressures may be written as:

$$\varepsilon_{ij} = \frac{(1+\nu)}{E}\sigma_{ij} - \frac{\nu}{E}\sigma_{kk}\delta_{ij} - \frac{\alpha_1}{3H}p\delta_{ij} \tag{4}$$

where E is elastic modulus and ν is Poisson ratio, α_1 and H are constants and will be discussed later and δ_{ij} is the Kronecker delta. The equilibrium equation in the absence of self weight and inertial effects may be given as:

$$\sigma_{ij,j} = 0 \tag{5}$$

and the strain-displacement relation is defined as:

$$\varepsilon_{ij} = \tfrac{1}{2}(u_{i,j} + u_{j,i}) \tag{6}$$

Governing equations

The equation governing solid body deformation is obtained through substitution of Eq. 4 and the strain-displacement relation of Eq. 6 into the equilibrium equation, Eq. 5, to yield, following some rearrangement (Biot, 1941):

$$Gu_{i,jj} + (\lambda + G)u_{k,ki} + \alpha_1 p_{,i} = 0 \tag{7}$$

where G is shear modulus and λ is a Lame constant. Darcy flow velocity, v_i can be expressed as:

$$v_i = Kp_{,i} \tag{8}$$

The basic statement of continuity of flow requires that the divergence of the flow velocity be equal to the rate of fluid accumulation per unit volume of space, therefore:

$$v_{i,i} = \alpha_1 \dot{\varepsilon}_{kk} - \alpha_2 \dot{p} \tag{9}$$

where α_1 corresponds to α and α_2 corresponds to $1/Q$ in Biot's theory (Biot, 1941). Substituting Eq. 8 into Eq. 9 gives the governing equation representing flow as:

$$-\frac{1}{\rho g} Kp_{,kk} = \alpha_1 \dot{\varepsilon}_{kk} - \alpha_2 \dot{p} \tag{10}$$

Equations 7 and 10 constitute the governing system equations for poroelastic behavior.

Parametric determination

In general, Terzaghi's effective stress law is defined as:

$$\sigma^e_{ij} = \sigma^c_{ij} - p\delta_{ij} \tag{11}$$

where σ^e_{ij} is effective stress, and σ^c_{ij} is total stress. The validity of Terzaghi's effective stress remains questionable, in particular for rock engineering since primary assumptions are of incompressible fluid and grains. Where grain compressibility is finite a stress ratio term must be added.

The two important parameters α_1 and α_2 used in Eqs. 7 and 10, require definition. In Biot's theory, the volumetric strain can be written as:

$$\theta = \frac{1}{K_s}\left(\frac{1}{3}(\sigma_{11} + \sigma_{22} + \sigma_{33}) - \frac{K_s}{H}p\right) \tag{12}$$

or for isotropic stress conditions:

$$\sigma_{11} + \sigma_{22} + \sigma_{33} = 3\sigma_c \tag{13}$$

$$\theta = \frac{1}{K_s}(\sigma_c - \alpha p) = \frac{1}{K_s}\sigma_e \tag{14}$$

The effective stress may be defined as:

$$\sigma_e = \sigma_c - \alpha p \tag{15}$$

where α is termed the pore pressure ratio. Equation 15 reduces to Terzaghi's theory only when α is unity. Although α may approach unity for compressible rocks (Kranz et al., 1979; Walsh, 1981), the magnitude may be determined from both the degree of rock fracturing and solid bulk modulus. Geertsma (1957) and Skempton (1960) proposed, on experimental grounds, that:

$$\alpha = 1 - \frac{K_s}{K_g} \tag{16}$$

where K_s is the effective modulus of the skeleton and K_g is the bulk modulus of grains. Nur and Byerlee (1971) verified this relationship theoretically. It is only when the effective compressibility of the dry aggregate is much greater than the intrinsic compressibility of the solid grains ($K_s \ll K_g$), that α and Eq. 15 reduce to the Terzaghi relationship of Eq. 11.

In Biot's approach (1941):

$$\alpha_1 = \frac{2(1+\nu)}{3(1-2\nu)}\frac{G}{H} = \frac{E}{3(1-2\nu)H} \tag{17}$$

$$\alpha_2 = \frac{1}{R} - \frac{\alpha_1}{H} \tag{18}$$

where R and H are constants that may be experimentally determined.

From the theory of elasticity (Timoshenko, 1934), it is known that bulk modulus of rock, K_s, has the form:

$$K_s = \frac{E}{3(1-2\nu)} \tag{19}$$

Equation 17 may be rewritten as:

$$\alpha_1 = \frac{K_s}{H} \tag{20}$$

Noting the equivalence of α_1 and α_2, and equating

Eq. 20 with Eq. 16, we have:

$$H=\left(\frac{1}{K_s}-\frac{1}{K_g}\right)^{-1} \tag{21}$$

It may be noted that only when $K_g \gg K_s$, $K_s \approx H$ (which is often the case for soil), that Terzaghi's effective stress law holds.

It is a more controversial issue to define the parameter α_2. In major part this results from the dispute with regard to the exact form of Terzaghi's effective stress law. If the effective stress law is followed, α_2 is most widely suggested to be (Verruijt, 1969; Bear, 1972; Huyakorn and Pinder, 1983):

$$\alpha_2=\frac{n}{K_f} \tag{22}$$

If the compressibility of the solid grains is not negligible however, then (Liggett and Liu, 1983):

$$\alpha_2=\frac{(1-n)}{K_s}+\frac{n}{K_f} \tag{23}$$

If we equate Eqs. 23 and 18 and also note Eqs. 20 and 21, then R may be derived for Biot's theory as follows:

$$R=\left(\frac{n}{K_f}+\frac{1-n}{K_g}+\frac{(K_g-K_s)^2}{K_s K_g^2}\right)^{-1} \tag{24}$$

Finite-element formulation

From the previous analysis, Eqs. 7 and 10 may be rewritten in two-dimensions as:

$$G\frac{\partial^2 u_i}{\partial x_j \partial x_j}+(\lambda+G)\frac{\partial^2 u_j}{\partial x_i \partial x_j}+\alpha_1\frac{\partial p}{\partial x_i}=0 \tag{25}$$

$$\frac{1}{\rho g}\frac{\partial}{\partial x_i}\left(K\frac{\partial p}{\partial x_i}\right)-\alpha_2\frac{\partial p}{\partial t}+\alpha_1\frac{\partial}{\partial t}\left(\frac{\partial u_i}{\partial x_i}\right)=0 \tag{26}$$

with $i=1,2$; $j=1,2$ and α_1 is defined in Eq. 17 with H being defined by Eq. 21. α_2 is referred to as relative compressibility and is defined in Eq. 18 with R being given by Eq. 24. When $K_s \ll K_g$, then:

$$R=\left(\frac{n}{K_f}+\frac{1}{K_s}\right)^{-1} \tag{27}$$

or: $\alpha_2 = n/K_f$.

Shape functions may be prescribed to map displacements and pressures:

$$u_i=\mathbf{N}\bar{u}_i \qquad p_i=\mathbf{M}\bar{p}$$

where $\bar{u}_i$ and $\bar{p}$ are nodal magnitudes of displacements and fluid pressures, $\mathbf{N}$ and $\mathbf{M}$ are element-based shape functions. The substitution of the shape functions and application of Galerkin's principle to Eq. 25 leads to:

$$\int_V\left\{\mathbf{N}G\frac{\partial^2\bar{u}_i}{\partial x_j\partial x_j}+(\lambda+G)\mathbf{N}\frac{\partial^2\bar{u}_j}{\partial x_i\partial x_j}+\alpha_1\mathbf{M}\frac{\partial\bar{p}}{\partial x_i}\right\}dV=0 \tag{28}$$

where V is the volume of the integral domain.

Applying Green's theorem to all derivative terms in Eq. 28, and using surface traction boundary conditions, the result may be rearranged in an incremental form after dividing through by time increment Δt:

$$\int_V\left\{G\frac{\partial\mathbf{N}}{\partial x_j}\left(\frac{\partial\mathbf{N}}{\partial x_j}\frac{\partial\bar{u}_i}{\partial t}+\frac{\partial\mathbf{N}}{\partial x_i}\frac{\partial\bar{u}_j}{\partial t}\right)+\lambda\frac{\partial\mathbf{N}}{\partial x_i}\frac{\partial\mathbf{N}}{\partial x_j}\frac{\partial\bar{u}_j}{\partial t}+\alpha_1\frac{\partial\mathbf{M}}{\partial x_i}\mathbf{M}\frac{\partial\bar{p}}{\partial t}\right\}dV=\int_S\mathbf{N}\frac{\partial\bar{f}_i}{\partial t}dS \tag{29}$$

where S is the domain surface upon which surface tractions $\bar{f}_i$ are applied as boundary conditions. In a similar manner, the flow relationship of Eq. 26 may be approximated using Galerkin's procedure, to give:

$$\int_V\left\{\frac{1}{\gamma}\frac{\partial\mathbf{M}}{\partial x_i}\mathbf{K}\frac{\partial\mathbf{M}}{\partial x_i}\bar{p}-\alpha_2\mathbf{M}^{\mathrm{T}}\mathbf{M}\frac{\partial\bar{p}}{\partial t}+\alpha_1\mathbf{N}\frac{\partial\mathbf{N}}{\partial x_i}\frac{\partial\bar{u}_i}{\partial t}\right\}dV=\int_S\mathbf{M}\bar{q}\,dS \tag{30}$$

where K is hydraulic conductivity, γ is fluid unit weight $\gamma=\rho g$ and $\bar{q}$ is the outward fluid flux specific discharge) normal to boundary surface, S.

Equations 29 and 30 can be written in matrix form as:

$$\begin{pmatrix}0 & 0\\ 0 & \mathbf{E}\end{pmatrix}\begin{pmatrix}\mathbf{u}\\ \mathbf{p}\end{pmatrix}+\begin{pmatrix}\mathbf{K}_{\mathrm{T}} & \mathbf{R}\\ \mathbf{R}^{\mathrm{T}} & \mathbf{L}\end{pmatrix}\begin{pmatrix}\dot{\mathbf{u}}\\ \dot{\mathbf{p}}\end{pmatrix}=\begin{pmatrix}\dot{\mathbf{F}}\\ \mathbf{Q}\end{pmatrix} \tag{31}$$

where:

$$\mathbf{u}=\{u_1,u_2\}^{\mathrm{T}}=\{u,v\}^{\mathrm{T}},\ \mathbf{p}=\{p\}$$

are vectors of nodal displacements and pressures, respectively, and:

$$\mathbf{E} = \frac{1}{\gamma}\int_V \frac{\partial \mathbf{M}}{\partial x_i}\mathbf{K}\frac{\partial \mathbf{M}}{\partial x_i}\,dV \tag{32}$$

$$K_T = \int_V \mathbf{B}^T\mathbf{D}\mathbf{B}\,dV \tag{33}$$

and **B** is the strain-displacement matrix:

$$\mathbf{B}^T = \begin{pmatrix} \frac{\partial}{\partial x_1} & 0 \\ 0 & \frac{\partial}{\partial x_2} \\ \frac{\partial}{\partial x_2} & \frac{\partial}{\partial x_1} \end{pmatrix} \tag{34}$$

$$\mathbf{D} = \frac{E}{(1+\nu)(1-2\nu)}\begin{pmatrix} 1-\nu & \nu & 0 \\ \nu & 1-\nu & 0 \\ 0 & 0 & \frac{1-2\nu}{2} \end{pmatrix} \tag{35}$$

$$\mathbf{R}^T = \int_V \alpha_1 \mathbf{N}\frac{\partial \mathbf{N}}{\partial \mathbf{x}_i}\,dV, \qquad \mathbf{R} = \int_V \alpha_1 \frac{\partial \mathbf{M}}{\partial x_i}\mathbf{M}\,dV \tag{36}$$

where $i = 1,2$.

$$\mathbf{L} = -\int_V \alpha_2 \mathbf{M}^T\mathbf{M}\,dV \tag{37}$$

$$\hat{\mathbf{F}} = \int_S \mathbf{N}\hat{\mathbf{f}}\,dS \tag{38}$$

$$\mathbf{Q} = \int_S \mathbf{M}q\,dS \tag{39}$$

Incompatible mode

For the governing equations (Eqs. 29 and 30) to be physically meaningful, it is essential that the components of the partial stress tensor be continuously differentiable to the first order. Thus, using polynomial interpolation functions (shape functions) the pore pressure distribution must be one order lower than that chosen for the displacement field. A quadratic displacement field and a linear pressure field are chosen in this work. For the choice of a rectangular element, quadratic representation can be accommodated by adding central nodes to the element. In order to achieve quadratic displacement representation and bilinear variation of pressure within individual elements, Turner's hybrid plane stress element (Turner et al., 1956) is incorporated into the finite-element program with the appropriate transformation for plane strain conditions. This hybrid element may be shown to create exactly the same stiffness matrix as Wilson's non-conforming element (Wilson et al., 1973; Froier et al., 1974).

In Turner's hybrid element, the corner displacement components are expressed as:

$$\begin{pmatrix} u \\ v \end{pmatrix} = \frac{1}{4}\begin{Bmatrix} N_1 & N_x & N_2 & -N_x \\ N_y & N_1 & -N_y & N_2 \end{Bmatrix} \begin{Bmatrix} N_3 & N_x & N_4 & -N_x \\ N_y & N_3 & -N_y & N_4 \end{Bmatrix} \begin{pmatrix} \bar{u}_i \\ \bar{v}_i \end{pmatrix} \tag{40}$$

where: $i = 1, 2, 3, 4$.

$$\begin{aligned} N_i &= (1+\eta_i\eta)(1+\psi_i\psi) \\ N_x &= \frac{av}{2b}(1-\eta^2) + \frac{b}{2a}(1-\psi^2) \\ N_y &= \frac{a}{2b}(1-\eta^2) + \frac{av}{2b}(1-\psi^2) \end{aligned} \tag{41}$$

where v is Poisson ratio, a and b are half width and half length of the four node element, and η and ψ are isoparametric mapping coordinates in the horizontal and vertical directions, respectively.

Time stepping schemes

In transient analysis, the discrete equations must be represented in the time domain. A simple two-point finite-difference discretization in time may be used instead of the finite-element approach since the increased accuracy obtained in using the latter method does not justify the additional computational effort.

To approximate the derivative of a function, u, with respect to t by a general finite-difference scheme, we have:

$$\dot{u} = \frac{u_{t+1} - u_t}{\Delta t} \tag{42}$$

To approximate an unknown function u, we can write:

$$u_{t+\chi t} = \chi(u_{t+1}) + (1-\chi)(u_t) \tag{43}$$

where χ is a weighting constant describing linear behavior within the time step Δt, $\chi = 1$ represents a forward or explicit discretization of time, $\chi = 0$ a backward or implicit finite-difference scheme and $\chi = 0.5$ a Crank–Nicolson or central difference scheme. It is well known that for an unconditionally stable finite-difference approximation, we should have $\chi \geqslant 0.5$.

Equation 29 may be rearranged as:

$$\mathbf{K}_T\dot{\mathbf{u}} + \mathbf{R}\dot{\mathbf{p}} = \dot{\mathbf{F}} \tag{44}$$

together with Eq. 30:

$$\mathbf{E}\dot{\mathbf{p}} + \mathbf{R}^t\dot{\mathbf{u}} + \mathbf{L}\dot{\mathbf{p}} = \mathbf{Q} \tag{45}$$

A matrix form of the backward time-stepping procedure is adopted in this analysis and may be written as:

$$\begin{pmatrix} \mathbf{K}_T & \mathbf{R} \\ \mathbf{R}^T & \Delta t\mathbf{E} + \mathbf{L} \end{pmatrix} \begin{pmatrix} \mathbf{u} \\ \mathbf{p} \end{pmatrix}^{t+1} = \begin{pmatrix} \mathbf{K}_T & \mathbf{R} \\ \mathbf{R}^T & \mathbf{L} \end{pmatrix} \begin{pmatrix} \mathbf{u} \\ \mathbf{p} \end{pmatrix}^{t} + \begin{pmatrix} \mathbf{F} \\ \Delta t\mathbf{Q} \end{pmatrix}^{t+1} + \begin{pmatrix} \mathbf{F} \\ \mathbf{0} \end{pmatrix}^{t} \tag{46}$$

For improved accuracy, using the Crank–Nicolson scheme, the following matrix form may be substituted:

$$\begin{pmatrix} \mathbf{K}_t & \mathbf{R} \\ \mathbf{R}^t & \frac{1}{2}\Delta t\mathbf{E} + \mathbf{L} \end{pmatrix} \begin{pmatrix} \mathbf{u} \\ \mathbf{p} \end{pmatrix}^{t+1} = \begin{pmatrix} \mathbf{K}_T & \mathbf{R} \\ \mathbf{R}^t & \mathbf{L} \end{pmatrix} \begin{pmatrix} \mathbf{u} \\ \mathbf{p} \end{pmatrix}^{t} + \begin{pmatrix} \mathbf{F} \\ \frac{1}{2}\Delta t\mathbf{Q} \end{pmatrix}^{t+1} + \begin{pmatrix} \mathbf{F} \\ \frac{1}{2}\Delta t\mathbf{Q} \end{pmatrix}^{t} \tag{47}$$

Initial conditions

It is assumed that in the interior of the porous medium displacements, u, and pore pressures, p, are continuous functions of space and time. In fact, this condition holds for the first differential coefficients with regard to t, and for the first and second differential coefficients with regard to x and y in governing equations 29 and 30. However, these assumptions cannot be made at the boundary of the porous medium, nor can they be made at the instant that loading is instantaneously applied. As a result, special treatments of boundary and initial conditions are required.

In general, the initial displacement field and pore pressure distribution can be evaluated through solving the static governing equation:

$$\begin{pmatrix} \mathbf{K}_T & \mathbf{R} \\ \mathbf{R}^T & \mathbf{L} \end{pmatrix} \begin{pmatrix} \mathbf{u} \\ \mathbf{p} \end{pmatrix} = \begin{pmatrix} \mathbf{F} \\ \mathbf{0} \end{pmatrix} \tag{48}$$

However, for incompressible or only slightly compressible fluid, the static governing equation may be ill-conditioned. An alternative method is to use a ramp loading as described in the following to approximate the initial conditions.

Instantaneous loading may be expressed as:

$$\begin{cases} f(t) = 0 & t < 0 \\ f(t) = f_0 & t \geq 0 \end{cases} \tag{49}$$

This leads to instantaneous generation of pore pressures and corresponding displacement field as shown in Fig. 1(a). The resulting discontinuity at time $t = 0$ should be smoothed to ensure a proper imposition of initial conditions. One method able to avoid violent oscillations that may result from step loading is to use a linear function in the first time step as illustrated in the following:

$$\begin{cases} f(t) = 0 & t < 0 \\ f(t) = f_0 t/\Delta t & 0 \leq t \leq \Delta t \\ f(t) = f_0 & t > \Delta t \end{cases} \tag{50}$$

This is illustrated in Fig. 1(b), where $f(t)$ represents the time-dependent nodal force.

Model validation

The finite-element model introduced previously has been validated against a number of published cases.

The first example involves the process of consolidation of a rock column subjected to a uniformly distributed external load q with the lateral motion being constrained. The finite-element configuration is shown in Fig. 2. The comparison of temporal settlement (surface subsidence) between the numerical model presented and the analytical equivalent

(a) Step function

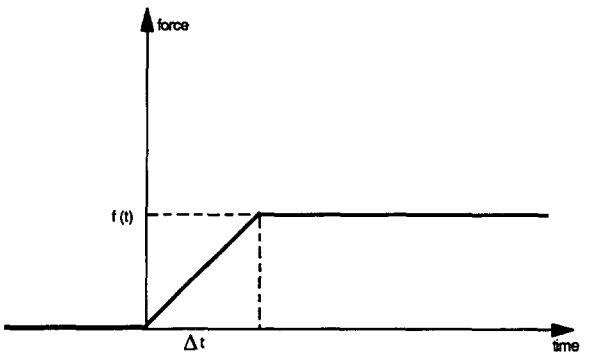

(b) Approximation function

Fig. 1. Force boundary.

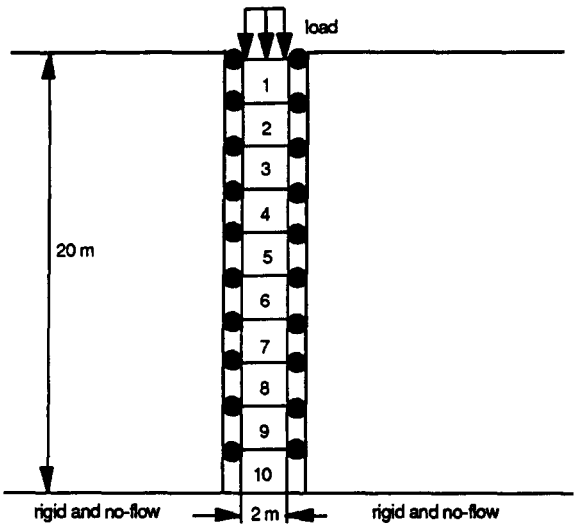

Fig. 2. Column problem by a finite-element model.

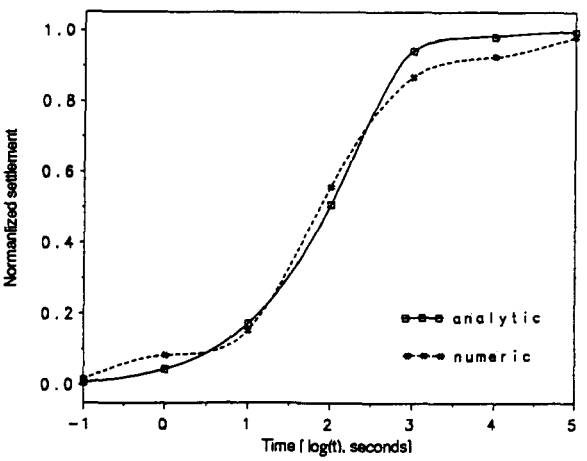

Fig. 3. Temporal settlement by column problem.

single porosity model by Biot (1941) is depicted in Fig. 3. It appears that good agreement is achieved except at late times.

It is frequently convenient to use a dimensionless time scale factor, T such as:

$$T=\frac{C_v t}{H_c^2} \tag{51}$$

where t is real time, H_c is height of the column, and coefficient of consolidation, C_v, may be evaluated through the following.

It is known from Biot consolidation theory (1941):

$$\alpha=\frac{2(1+v)G}{3(1-2v)H}=\frac{E}{3(1-2v)H}=\frac{K_s}{H} \tag{52}$$

where H is defined in Eq. 21. Therefore, Eq. 16 holds ($\alpha_1=\alpha$).

Biot (1941) defined:

$$\frac{1}{Q}=\frac{1}{R}-\frac{\alpha}{H} \tag{53}$$

Substituting Eqs. 16, 21 and 52 into 53, yields:

$$\frac{1}{Q}=\left\{\frac{(K_g-K_s)^2}{K_s K_g^2}+\frac{1-n}{K_g}+\frac{n}{K_f}\right\}^{-1} -\left(1-\frac{K_s}{K_g}\right)\left(\frac{1}{K_s}-\frac{1}{K_g}\right) \tag{54}$$

If we assume $K_g \simeq K_s$, $K_g \gg 1$, then:

$$\frac{1}{Q} = \frac{1}{\frac{1}{K_s} + \frac{n}{K_f}} - \frac{1}{K_s} \tag{55}$$

For the condition $Q = \infty$, as defined for saturated clay in Biot (1941), we have:

$$K_s = \frac{1}{2}\left\{\frac{n}{K_f} \pm \sqrt{\frac{n^2}{K_f^2} + 4}\right\} \tag{56}$$

where only skeletal compressibility is accommodated. From Biot (1941):

$$\alpha^* = \frac{1-2\nu}{2G(1-\nu)} = \frac{(1+\nu)(1-2\nu)}{(1-\nu)E} \tag{57}$$

and:

$$\frac{1}{C_v} = \left(\frac{a^*}{K} + \frac{1}{QK}\right)\rho g \tag{58}$$

where K is hydraulic conductivity (permeability coefficient). Substituting Eq. 57 into 58 and rearranging the result, gives:

$$C_v = K\left\{\frac{(1+\nu)(1-2\nu)}{(1-\nu)E} + \frac{1}{Q}\right\}^{-1}\frac{1}{\rho g} \tag{59}$$

If $Q = \infty$ then:

$$C_v = \frac{E(1-\nu)}{(1+\nu)(1-2\nu)}K\frac{1}{\rho g} \tag{60}$$

Equation 60 has been used widely (Biot, 1941; Ghaboussi and Wilson, 1973; Khaled et al., 1984; Booker and Small, 1987).

A comparison of excess pore pressure along the column of Fig. 2 is made between this numerical model and the analytical solution proposed by Terzaghi (1923). Dimensionless time factor, T, is calculated from Eq. 51. The results are shown in Fig. 4 and a relatively good match is achieved except at the nodes close to the loading surface due to numerical instability.

Another example is given for a two-dimensional problem comprising a layered geometry. A rock layer of depth H_c is subjected to a uniformly

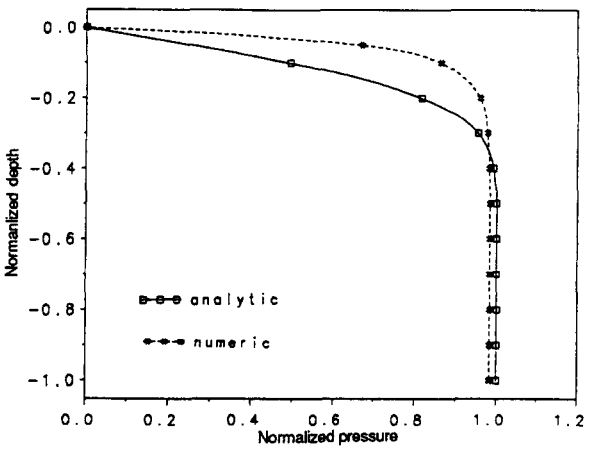

Fig. 4. Spatial pore pressure by column problem.

applied load, q, of width a^*. The surface is freely drained, the bottom is rigid and the mesh is shown in Fig. 5. Dimensionless time, T, may be evaluated using Eq. 51. For a ratio of H_c/a^* equal 1, the normalized surface settlement of the model described in this work is depicted in Fig. 6 and is compared with the calculation by Booker (1974) for the case of $\nu = 0$. A satisfactory match is achieved.

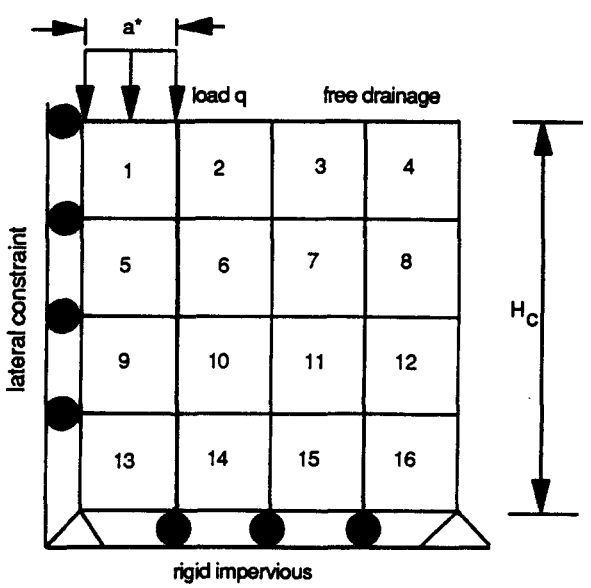

Fig. 5. Mesh layout for a 2-D finite-element model.

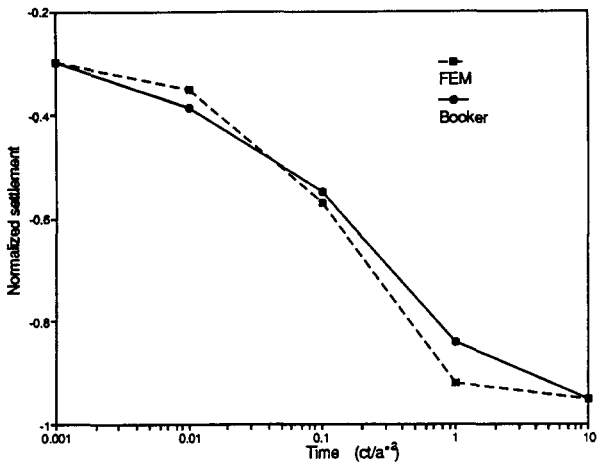

Fig. 6. Temporal surface settlement.

Model applications

The transient poroelastic model has a number of interesting applications in predicting the time-dependent solid displacement and fluid pressure response of porous media as a result of underground mining. A steady-state model may be valid in simulating the terminal change in fluid pressure. For evaluating a change in the fluid pressure as mining progresses, application of a transient model appears mandatory.

The model described previously is used to represent the response to underground mining of a horizontal panel in an elastic medium. Excess pore pressure is assumed to be zero everywhere, initially. In representing behavior resulting from underground excavation, a force boundary condition equivalent to cover load is applied at the mining level to generate an elastic displacement field as well as a resulting pore pressure field in the surrounding rock. Excess pore pressures are retained as zero on the surface, in the far field and equivalent to negative hydrostatic pressure on the excavation boundary. Advantage is taken of model symmetry, with only half of the model represented in the lateral direction, starting from the centerline of the panel where nodes are allowed to move vertically only.

In the following, subsidence is reported first, followed by the description of pore pressure effects. In each of these sections, instantaneous excavation is first considered followed by the discussion of progressive excavation.

Time-dependent surface displacements

The coupling between elastic displacement and fluid pressure under external loading can be described by the process of consolidation, in which a gradual increase of solid displacement occurs as a consequence of fluid pressure dissipation due to drainage at the mine opening. An explicit view of the longitudinal and transverse sections of a longwall panel examined here is depicted in Fig. 7.

(a) Surface displacement in transverse section (instantaneous excavation)

The initial displacement of the porous medium in this particular problem is large as a result of the elastic compressibility of the system. The duration of consolidation is short as controlled by the fluid diffusive parameters of the system. An illustrative finite-element mesh layout (model a) is given in Fig. 8 for a transverse section where model symmetry has been considered. Parameters averaged from field measurements for this particular case study are described in Table 1.

Normalized surface subsidence over the mining panel with respect to various times is depicted in Fig. 9. Rapid consolidation may be noted with the curves illustrating an abrupt increase in surface subsidence, in particular over the gob centers. This

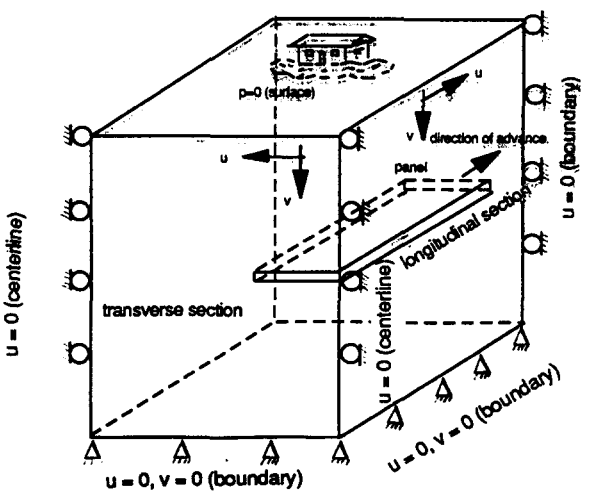

Fig. 7. Three-dimensional view of a longwall panel.

TABLE 1

Parameters for finite-element model a

Material	Conduct(gpd/ft^2)	Modulus(psf)	Poisson ratio
1	1	500000	0.25
2	0.5	5000	0.4
3	0.6	200000	0.3

Conversion: 1 gpd/ft^2 = 4.72×10^{-7} m/s and 1 psf = 47.88 Pa.

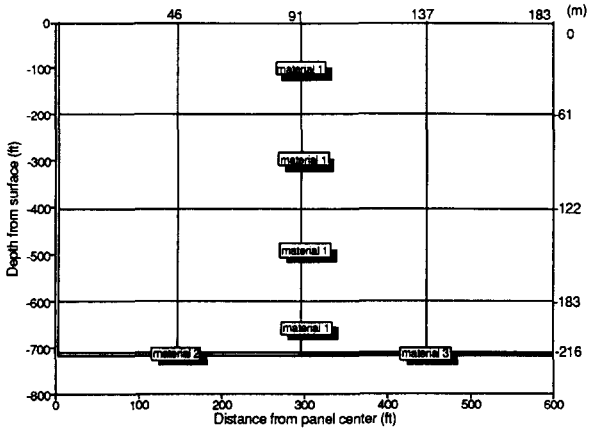

Fig. 8. Mesh layout for finite-element model a.

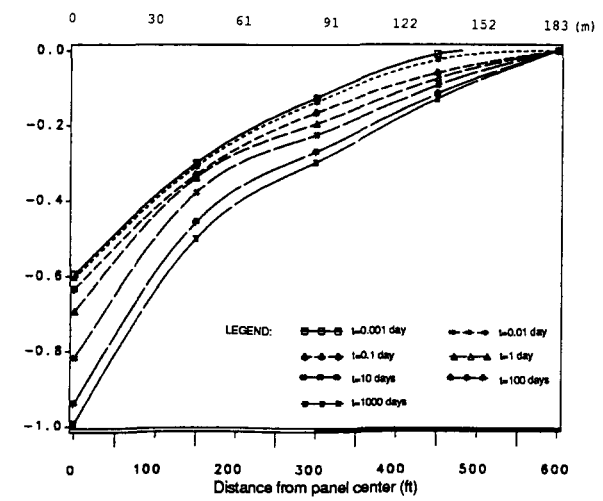

Fig. 9. Temporal surface subsidence for model a.

may reflect the effect of a strong contrast in material properties between the gob and the surrounding strata.

The predicted surface horizontal displacement is illustrated in Fig. 10. The maximum horizontal

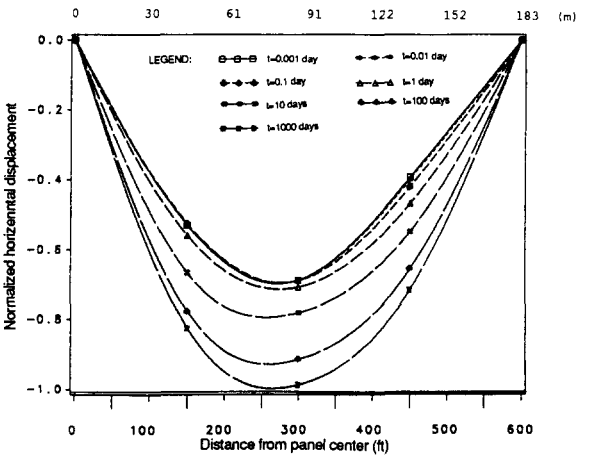

Fig. 10. Temporal surface horizontal displacement for model a.

displacement occurs approximately 250 ft (76.2 m) from the panel center. This is an indication that maximum surface slope occurs within the area directly over the gob.

(b) Surface displacement in longitudinal section (progressive excavation)

Transient surface displacement is apparently critical in the longitudinal direction as the mining face advances. A correct prediction of the travelling subsidence wave ahead of mine development may result in the recognition of an efficient treatment to minimize potential damage due to mining.

The advance rate of the mining face, however, is usually not a continuous function of time. There is often downtime, delay time, and even accidents that prevent the face from moving continuously. For a first approximation, however, a constant rate of face advance is assumed in this study. The finite-element mesh (model b) is given in Fig. 11. The material constants used in the model are listed in Table 2 (data are modified from the case study by Hasenfus et al., 1988).

The average rate of face advance is assumed to be 30 ft/day (9.1m /day). Behavior is viewed at times of 20, 40, 60 and 80 days, corresponding to 600, 1200, 1800 and 2400 ft advance (183, 366, 549, 732 m), respectively. The four stages of face advance is shown in Fig. 11. The loading is applied instantaneously at these designated times and locations as an approximation to smooth advance. The normalized travelling vertical displacement curves

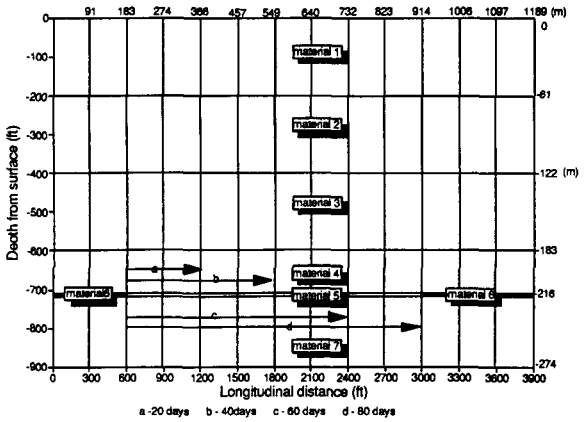

Fig. 11. Mesh layout for finite-element model b.

TABLE 2

Parameters for finite-element models b,c,d

Material	Conduct(gpd/ft^2)	Modulus(psf)	Poisson ratio
1	4.26	251000	0.27
2	0.33	868000	0.18
3	0.4	460000	0.22
4	1.12	460000	0.22
5	0.5	189000	0.37
6	0.3	50000	0.4
7	0.83	537000	0.2

Conversion: 1 gpd/ft^2 = 4.72×10^{-7} m/s and 1 psf = 47.88 Pa.

are shown in Fig. 12. The increase in size of the subsidence trough, both in depth and in extent, may be a direct consequence of both the increase in panel width and consolidation of the solid.

Transient pore pressure response

Variation of effective stress and thus pore pressure may exhibit a controlling influence over the modification of hydraulic conductivity, especially where the formation is fracture dominated. Pore pressures vary most in regions of large modification in total stresses. This poroelastic model is linear and does not account for changes in hydraulic conductivity. The behavior for instantaneous excavation of a 600 ft wide panel is examined in the following sections.

(a) Pore pressure in transverse section (instantaneous excavation)

A finite-element mesh (model c), similar to but denser than the one shown in Fig. 8 is depicted in Fig. 13, where the half mining width is 300 ft (91.4 m). The left side boundary represents the centerline of a mining panel. The parameters used in the calculation are given in Table 2.

Dissipative pore pressures are illustrated in Figs. 14–17 with respect to time, ranging from 1 day to 1000 days. Excess pore pressures in these figures are normalized with respect to the maximum pore pressure values in the time equal to 1 day. It is interesting to note that at earlier times (Fig. 14) the zones of high normalized excess pore pressure are located in the areas adjacent to the panel with the highest pressure magnitudes appearing around the panel perimeter near the abutment zone. The rapid change of the excess pressure profile can also be observed along the centerline of the gob. As time progresses, the pore pressure distribution in the vicinity of the opening changes sharply, with high pore pressure expanding to a larger region. The relatively higher pressure gradient in the panel areas is rapidly dissipating to the far field. At a time of 1000 days (Fig. 17), the general excess pressure distribution together with its magnitude does not vary noticeably in the domain (Fig. 17). At the time of 1000 days, the excess pore pressure is less than 1% of the initial value, and appears to be distributed almost uniformly compared with the initial pattern.

(b) Pore pressure in longitudinal section (progressive excavation)

The finite-element mesh (model d) shown in Fig. 18 is used, assuming the left boundary as the centerline of the mining panel. The parameters in Table 2 are applied again.

Assuming that the rate of face advance is 30 ft/day, the pore pressure distribution at four stages of mining for mining lengths equal to 600, 1200, 1800 and 2400 ft (183, 366, 549 and 732 m) are illustrated in Figs. 19–20, respectively, corresponding to 40, 80, 120 and 160 days in full mining width as depicted in Fig. 18. It is apparent that the induced pore pressure expands primarily in the horizontal direction as panel length increases. The

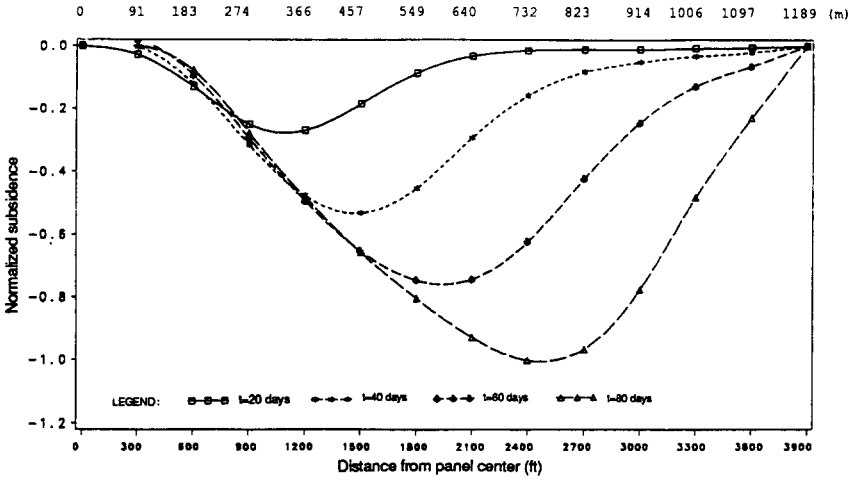

Fig. 12. Temporal subsidence profiles for model b.

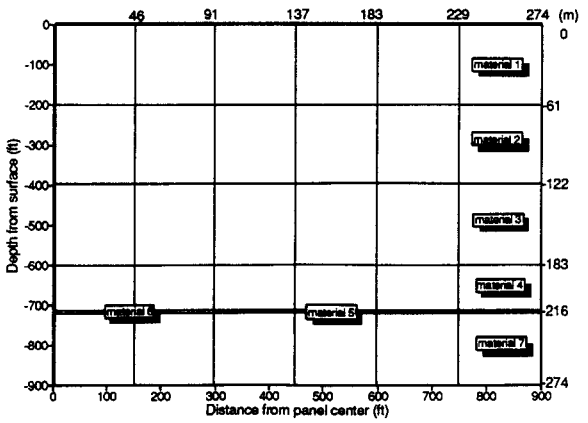

Fig. 13. Mesh layout for finite-element model c.

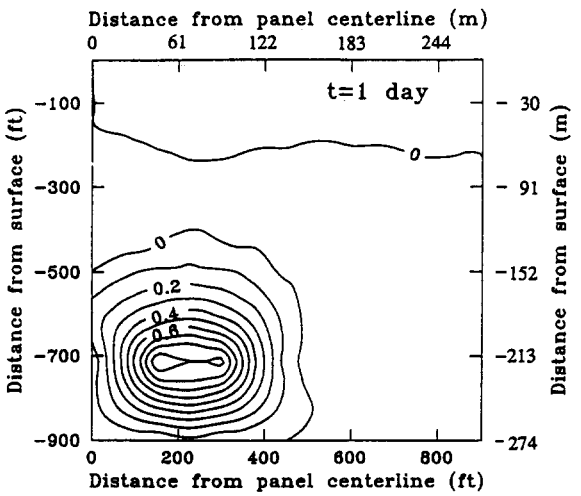

Fig. 14. Normalized pore pressure ($t = 1$ day).

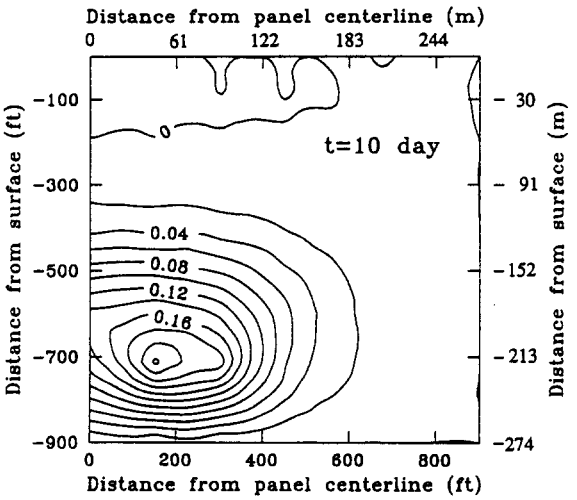

Fig. 15. Normalized pore pressure ($t = 10$ days).

major impact of mining appears to occur in the vicinity of the mining panel. High pore pressure occurs mainly in the region around the abutment zone in the neighborhood of gob. The generation of the significant pore pressure is obviously associated with the mining-induced high compressive stress in the mining region. This scenario is manifest where the half mining length reaches 1800 ft (548.6 m) in Fig. 22.

Further parametric investigation

From the previous analysis, the important parameters have been identified as the pore pres-

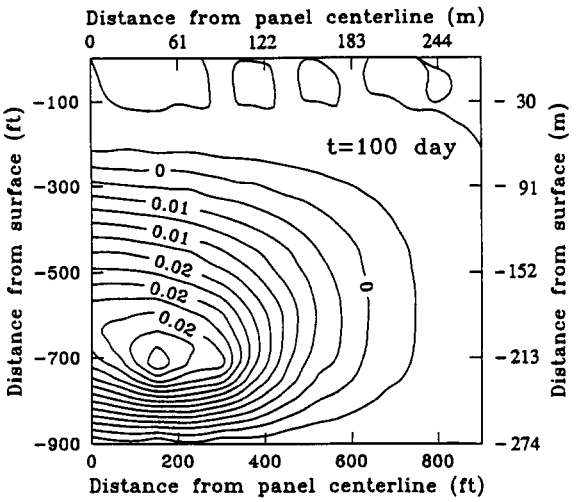

Fig. 16. Normalized pore pressure ($t = 100$ days).

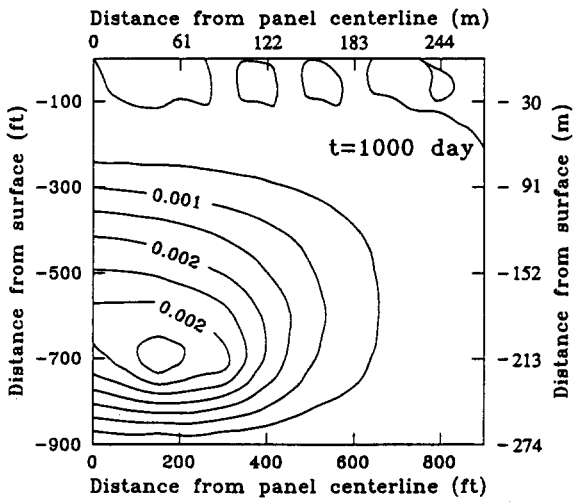

Fig. 17. Normalized pore pressure ($t = 1000$ days).

sure ratio α_1, and the relative compressibility, α_2. Further investigation of the effect of these parameters on pore pressure variation is described in the following, using the finite-element mesh (model c) illustrated in Fig. 13 and representing instantaneous excavation of a long tabular opening.

(a) Rate of pore pressure dissipation

Figure 23 depicts a rapid pore pressure dissipation over time along the centerline of the panel. It is found, however, that the dissipation rate may be substantially reduced by reducing the relative

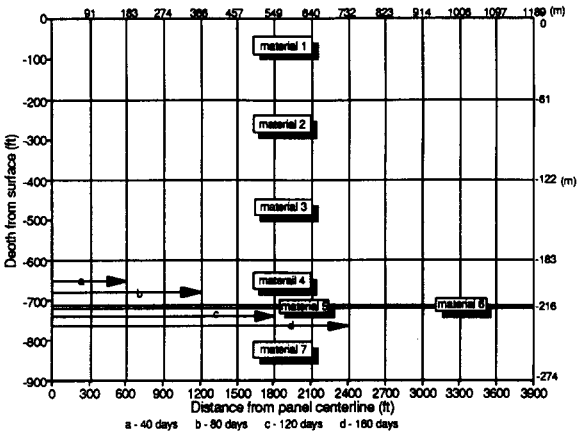

Fig. 18. Mesh layout for finite-element model d

compressibility α_2. It is of interest to note the dramatic change of fluid pressure throughout the overburden at time equal to 1 day, and around the mining region at time equal to 10 days. Excess pore pressure declines fast after 10 days and diminishes at time equal to 1000 days.

(b) Pore pressure ratio

The pore pressure ratio, α_1,indexes the relative impact of the seepage force on resulting solid body deformations. For a relative compressibility α_2 equal to 0.001, Figure 24 indicates the normalized fluid pressure at the point of 600 ft (183 m) from the panel centerline and at the depth of 720 ft (219 m) between the time of 0.01 day and 100 days, with α_1 ranging between 0.5 and 1. There is no striking difference between various α_1 magnitudes although a higher α_1 in general represents a higher induced pressure field. It appears that the effect of the pore pressure ratio is unimportant in terms of the evaluation of fluid pressure magnitudes, at least under these particular circumstances.

(c) Relative compressibility

For a constant porosity and constant pore pressure ratio α_1, relative compressibility, α_2, is inversely proportional to the fluid bulk modulus and solid bulk modulus. For an α_1 of 1.0 and at the depth 200 ft along centerline, the sensitivity of pore pressures against various α_2's is depicted in Fig. 25 between times 0.01 day to 100 days. A

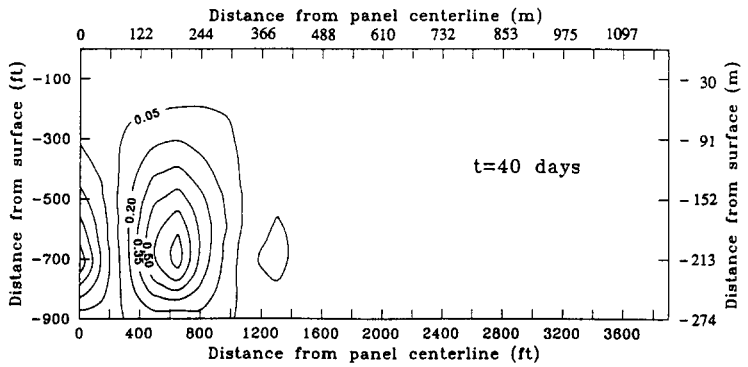

Fig. 19. Normalized pore pressure along longitudinal direction ($t = 40$ days).

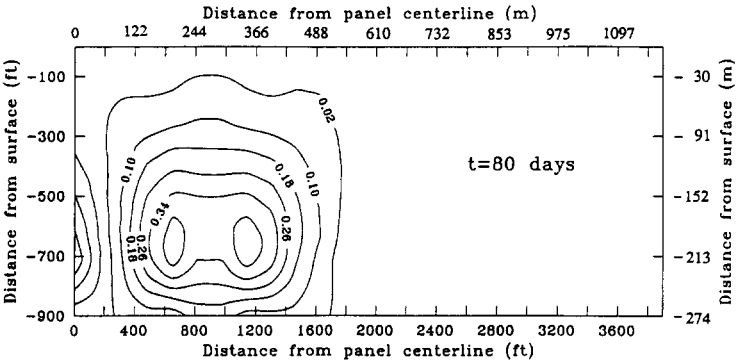

Fig. 20. Normalized pore pressure along longitudinal direction ($t = 80$ days).

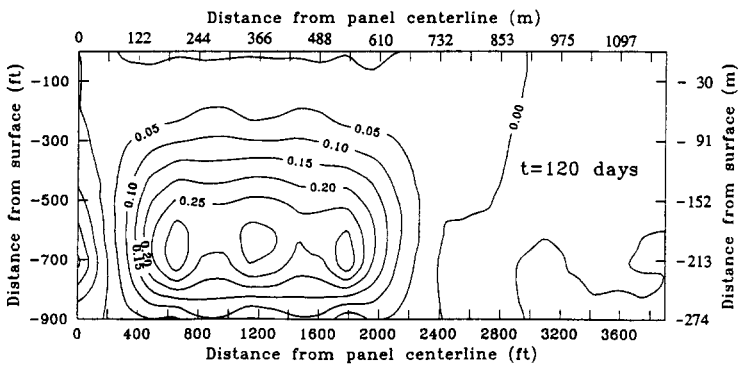

Fig. 21. Normalized pore pressure along longitudinal direction ($t = 120$ days).

dramatic reduction of pore pressure occurs when α_2 increases from 0.005 to 0.05. The rate of the pressure change is reduced if α_2 is larger than 0.025. A greater compressibility of the porous medium results in a smaller pore pressure being generated along the panel centerline, probably due to an increase in displacement field. This scenario holds equally with constant bulk modulus but variable porosity.

Concluding remarks

A finite-element model representing single porosity poroelasticity is presented and utilized in

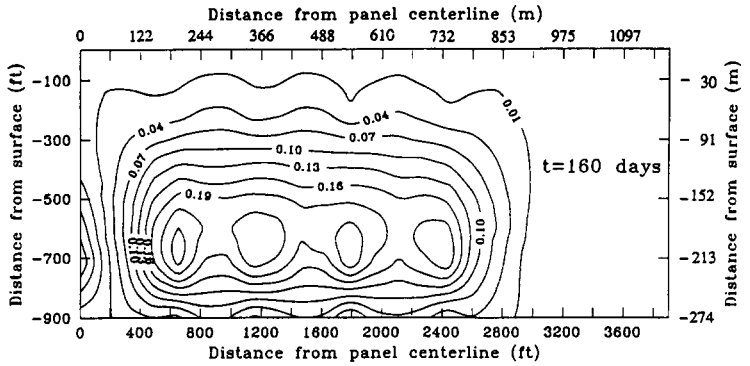

Fig. 22. Normalized pore pressure along longitudinal direction ($t = 160$ days).

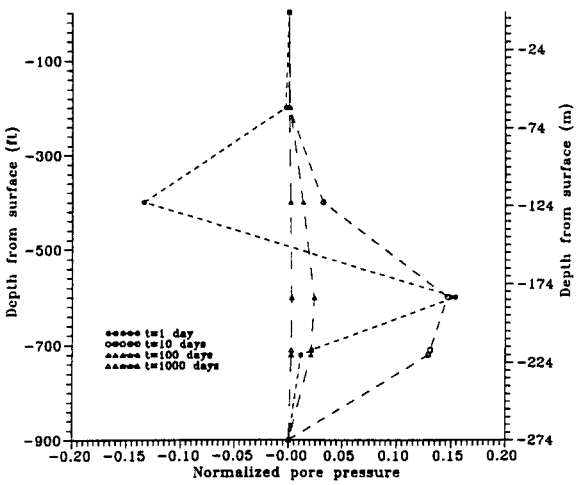

Fig. 23. Normalized pore pressure over centerline.

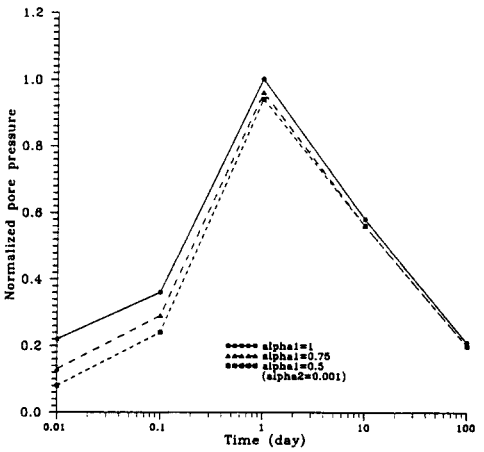

Fig. 24. Normalized pore pressure at 720 feet below surface on centerline.

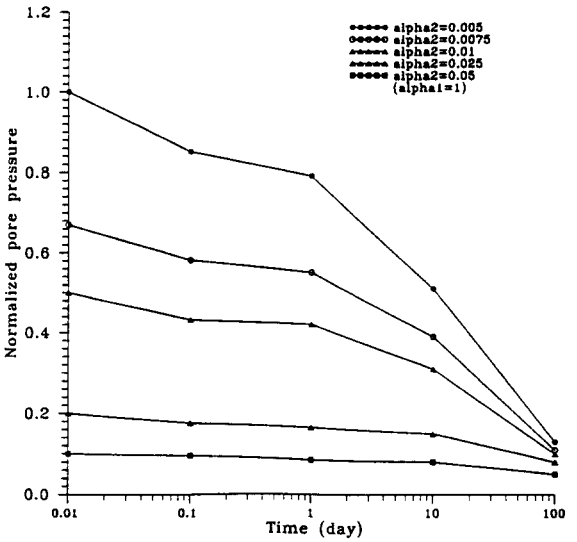

Fig. 25. Normalized pore pressure at 200 feet below surface on centerline.

particular to investigate the transient behavior around underground longwall panels. The following conclusions may be drawn as a result of this analysis.

(a) In some poroelasticity models, the pore pressure ratio α_1 is assumed to be unity, as suggested by Terzaghi (1923). However, both experimental studies (Geertsma, 1957; Skempton, 1960) and theoretical analyses (Nur and Byerlee, 1971) have indicated that α_1 may approach unity only when the bulk modulus of the grains is significantly greater than that of the skeleton of the porous medium. This may be true for soil, but is rarely true for most rocks. The magnitude of α_1 represents the influence of the seepage force on the resulting

pressure and displacement field. A direct proportionality between α_1 and induced excess pore pressure is identified in this study. A decrease in the pore pressure ratio, α_1, results in a reduction in induced pore fluid pressures. For the material characteristics used in this study, pore pressures appear insensitive to the ratio α_1.

(b) A significant change of the pore pressure field in the overlying strata during the mining process indicates that a substantial modification of hydraulic conductivity could occur. This change is not accommodated in the model. The prediction of this transient process may prove useful in minimizing adverse impact when mining is underway.

(c) The compressibilities of interstitial fluid and the solid skeleton appear inversely related to the magnitude of induced pore pressures. A greater change in pore pressures may occur in a porous medium with smaller relative compressibility.

(d) Time factor has a critical influence on the fluid pressure field and solid displacement field. The pore pressures dissipate with time. This transient response should be regarded as important in representing changes in the distribution of hydraulic conductivities during the mining process.

Acknowledgements

The authors would like to express their appreciation for the useful comments and suggestions from professor L.W. Saperstein. The appreciation is also extended to Dr. Kalkani for his critical review of the previous manuscript. The financial assistance from the Pennsylvania Energy Development Authority and data received from the Consolidation Coal Company are gratefully acknowledged.

References

Bear, J., 1972. Dynamics of Fluids in Porous Media. American Elsevier, New York, N.Y., 764 pp.

Biot, M.A., 1941. General theory of three dimensional consolidation. J. Appl. Phys., 12:. 155–164.

Booker,J.R., 1974. The consolidation of a finite layer subject to surface loading. Int. J. Solids Struct., 10: 1053–1605.

Booker, J.R. and Small, J.C., 1974. A method of computing the consolidation behaviour of layered soils using direct numerical inversion of Laplace transforms. Int. J. Num. Anal. Methods Geomech., 11: 363–380.

Detournay, E. and Cheng, A.H-D., 1988. Poroelastic response of a borehole in a non-hydrostatic stress field. Int. J. Rock Mech. Min. Sci. Geomech. Abstr., 25(3): 171–182.

Froier, M., Nilson, L and Samuelsson T., 1974. The rectangular plane stress element by Turner, Pian and Wilson, Int. J. Numer. Mech. Eng., 8(2): 433–437.

Ghaboussi, J. and Wilson, E.L., 1973. Flow of compressible fluid in porous elastic media. Int. J. Num. Methods Eng., 5: 419–442.

Geertsma, J., 1957. The effect of fluid pressure decline on volumetric changes of porous rocks. Trans. AIME, 331–340.

Hasenfus, G.J., Johnson, K.L. and Su, D.W.H., 1988. A hydrogeomechanical study of overburden aquifer response to longwall mining. Proc. 7th Int. Conf. Ground Control in Mining, Morgantown, W.V., pp. 149–162.

Huyakorn, P.S. and Pinder, G., 1983. Computational Methods in Subsurface Flow. Academic Press, New York, N.Y., 473 pp.

Lewis, R.W. and Schrefler, B.A., 1987. The Finite Element Method in the Deformation and Consolidation of Porous Media. Wiley, Chichester, 344 pp.

Liggett, J.A. and Liu, P.L.F., 1983. The Boundary Integral Equation Method for Porous Media Flow. George Allen & Unwin, London, 255 pp.

Khaled, M.Y., Beskos, D.E. and Aifantis, E.C., 1984. On the theory of consolidation with double porosity — Part 3, a finite element formulation, Int. J. Numer. Anal. Methods Geomech., 8: 101–123.

Kranz, R.L., Frankel, A.D., Engelder, T. and Scholz, C.H., 1979. The permeability of whole and jointed Barre granite, Int. J. Rock. Mech. Min. Sci. Geomech. Abstr., 16(3): 225–234.

Nur, A. and Byerlee, J.D., 1971. An exact effective stress law for elastic deformation of rock with fluids, J. Geophys. Res., 76(26): 6414–6419.

Simon, B.R., Zienkiewicz, O.C. and Paul, D.R., 1984. An analytical solution for the transient response of saturated porous elastic solids, Int. J. Num. Anal. Methods Geomech., 8: 381–398.

Skempton, A.W., 1960. Effective Stress in Soils, Concrete and Rock, Pore Pressure and Suction in Soils. Butterworths, London, pp. 4–16.

Terzaghi, K.V., 1923. Die Berechung der Durchassigkeitsiffer des Tones Aus dem Verlauf der hydrodynamischen Spannungserscheinungen, Sitzungsber. Akad. Wiss. Wien Math. Naturwiss. KI., Abt. 2A, 132: 105.

Timoshenko, S., 1934. Theory of Elasticity, 1st ed. McGraw-Hill, New York, N.Y., 416 pp.

Turner, M.J. Clough, R.W., Martin, H.C. and Topp, L.J., 1956. Stiffness and deflection analysis of complex structures, J. Aeronaut. Sci., 23: 8805–8823.

Verruijt, A., 1969. An Elastic Storage of Aquifers, Flow Through Porous Media. Academic press, New York, N.Y., pp. 331–376.

Walsh, J.B., 1981. Effect of pore pressure and confining pressure on fracture permeability, Int. J. Rock. Mech. Min. Sci. Geomech. Abstr., 18(3): 429-435.

Wilson, E.L., Taylor, R.L., Doherty, W. and Ghaboussi, J., 1973. Incompatiable displacement models. Int. Symp. Num. Comp. Meth. Struct. Mech., Academic Press, New York, N.Y., pp. 43–57.

Zienkiewicz, O.C., Humpheson, C. and Lewis, R.W., 1977. A unified approach to soil mechanics problems. In: G. Gudehus (Editor), Finite Element in Geomechanics. Wiley, Chichester, pp. 151–177.